

Research Article

MXene-derived TiO₂ nanosheets/rGO heterostructures for superior sodium-ion storage

 Baosong Li^{a,*}, Dezhuang Ji^b, Abdallah Kamal Hamouda^b, Shaohong Luo^c
^a Department of Aerospace Engineering, Khalifa University of Science and Technology, Abu Dhabi 127788, UAE

^b Department of Mechanical and Nuclear Engineering, Khalifa University of Science and Technology, Abu Dhabi 127788, UAE

^c Department of Biomedical Engineering, Khalifa University of Science and Technology, Abu Dhabi 127788, UAE

ARTICLE INFO

Keywords:

 Ti₃C₂T_x MXene
 Titanium dioxide
 Self-assembly
 Heterostructure
 Sodium-ion batteries

ABSTRACT

Transition metal oxides hold promise as electrode materials for energy-storage devices such as batteries and supercapacitors. However, achieving ideal electrode materials with high capacity, long-term cycling stability, and superb rate capability remains a challenge. In this study, we present a self-assembled heterogeneous structure consisting of TiO₂ nanosheets derived from Ti₃C₂T_x MXene and reduced graphene oxide. This structure facilitates the formation of heterogeneous structures while establishing a conductive network. The restacking of porous TiO₂ nanosheets and reduced graphene oxide within the heterostructure results in high porosity and excellent conductivity. Due to enhanced electron and Na⁺ transfer, as well as improved structural stability during the Na⁺ insertion/extraction process, this heterogeneous structure exhibited exceptional Na⁺ storage performance. Specifically, it exhibits a long-term cycling stability (217 mAh g⁻¹ at 10 C, 5000 cycles) and an ultrahigh rate capability (135 mAh g⁻¹, 40 C). Analysis of electrode reaction kinetics suggests that Na⁺ storage in the heterostructure is predominantly governed by a surface-controlled process. Our results provide a promising strategy for utilizing self-assembled heterostructures in advanced energy storage applications.

1. Introduction

Due to the energy crisis and growing concerns over environmental pollution, renewable energy systems have recently flourished, owing to their eco-friendly and inexhaustible characteristics. However, renewable energy sources such as solar, wind, and tidal energies are intermittent by nature, thereby limiting their function as consistent energy sources. Therefore, the development of stable and high-efficiency energy-storage techniques is highly needed to address the intermittency of renewable energy sources. Sodium-ion batteries (SIBs) are considered a highly competitive and efficient technology offering satisfying energy storage at a low cost [1,2]. The growing interest in SIBs has spurred extensive research into various materials to identify suitable electrodes with higher energy/power densities, as well as long-term stability. Various materials, including oxides [3,4], sulfides [5,6], selenides [7,8], carbides [9], phosphides [10,11], phosphorus [12,13], and carbon materials [14–16], have exhibited remarkable performance in Na⁺ storage. However, sluggish Na⁺ diffusion kinetics remain a significant obstacle to their widespread application [17,18].

On the basis of the insertion mechanism, TiO₂ has been recognized as a promising anode material for SIBs owing to its abundant resources, eco-friendliness, structural stability, as well as remarkable electrochem-

ical performance [19,20]. However, despite the numerous advantages, TiO₂ anodes exhibit poor electrical conductivity, low Na⁺ storage capacity, and sluggish Na⁺ diffusion kinetics [21]. Various approaches are employed to enhance the Na⁺ storage of TiO₂ anodes, including reducing the crystal size to the nanoscale (nanosphere [22], nanotube [23], and nanosheets [24]) to increase the active sites and reduce the Na⁺ diffusion paths. Additionally, introducing conductive materials to TiO₂ is a promising strategy to overcome this challenge [25–27].

Ti₃C₂T_x MXene has recently garnered significant attention owing to its high electrical conductivity, flexibility, abundant surface terminations, and ease of processing [28–30]. Recent studies have used Ti₃C₂T_x to generate nanostructured TiO₂ materials [31–33], whereas MXene-derived TiO₂ materials have shown significant potential in catalysis [31], energy storage [32], and electronics [33]. However, the poor stability of Ti₃C₂T_x MXene, particularly its rapid degradation in aqueous solutions under ambient conditions, leads to structural damage and loss of its desirable properties [34,35].

In this study, we propose a self-assembling strategy to prepare Ti₃C₂T_x MXene-derived TiO₂ nanosheets/reduced graphene oxide (denoted as TiO₂/rGO) heterostructures, using rGO as the electrically conductive layer and the derived TiO₂ nanosheets (denoted as TiO₂-NSs) as the main Na⁺ storage layer. The mesoporous TiO₂ nanosheets are

* Corresponding author.

 E-mail address: baosong.li@ku.ac.ae (B. Li).

supported by ultrathin N-doped graphene to form a heterogeneous structure. The prepared TiO₂/rGO heterostructures exhibited a self-assembled structure with abundant interfaces between TiO₂ and rGO, enhancing the electrolyte permeation within the electrode and maintaining the structural stability. Furthermore, the porous 2D structure of the prepared heterostructures shortens the Na-ion diffusion pathways and significantly improves the charge transfer kinetics, while the conductive graphene fastens electron transport and improves structural stability. Based on the aforementioned advantages, the TiO₂/rGO hybrids exhibited remarkable Na⁺ storage properties with a superior rate capability (40 C, 135 mAh g⁻¹) and long-term cycling stability (5000 cycles at 10 C).

2. Experimental section

2.1. Chemicals

Lithium fluoride (LiF, 99%) and poly(diallyldimethylammonium chloride) (PDDA, 20%) were purchased from Sigma-Aldrich Co., Ltd. Hydrochloric acid (HCl, 37%) was provided by Merck. MAX (Ti₃AlC₂, ≤40 μm) was purchased from Carbon-Ukraine Ltd. Graphene oxide (GO, 4 mg/mL) was obtained from Graphenea Inc. Deionized (DI) water was produced using a Milli-Q Biocel system.

2.2. Synthesis of Ti₃C₂T_x nanosheets

Ti₃AlC₂ (MAX phase) powders were selectively etched to prepare exfoliated Ti₃C₂T_x MXene following our previously reported methods [30,36]. Briefly, the etchant solution was prepared by dissolving lithium fluoride (1.6 g) into an HCl solution (9 M, 20 mL) in a plastic vessel. Then, the Ti₃AlC₂ powder (≤40 μm, 1 g) was gradually added to the etchant solution, followed by stirring at 35 °C for 24 h. After the etching process, the mixture was washed using DI water until a stable Ti₃C₂T_x suspension (pH ≈ 6) was achieved. The Ti₃C₂T_x MXene suspension was collected through centrifugation at 3500 r/min for 40 min.

2.3. Preparation of Ti₃C₂T_x-derived TiO₂ nanosheets

The concentrated Ti₃C₂T_x suspension was further diluted to 1 mg/mL using DI water to prepare the diluted Ti₃C₂T_x suspension. The diluted Ti₃C₂T_x suspension was treated with liquid nitrogen in a glass beaker and subjected to freeze-drying for 24 h. Subsequently, the freeze-dried Ti₃C₂T_x MXene was annealed at 450 °C (1 °C/min) for 10 h. Once cooled to room temperature, the white TiO₂ nanosheets (TiO₂-NS) were obtained.

2.4. Synthesis of PDDA-modified TiO₂ nanosheets

The TiO₂ nanosheets were first dispersed in DI water to obtain a TiO₂ suspension (0.5 mg mL⁻¹). Subsequently, a specific amount of diluted PDDA solution (0.5 wt%) was added to the TiO₂ suspension (1:40, weight ratio). The mixture was stirred for 3 h to obtain PDDA-modified TiO₂ nanosheets.

2.5. Assembly of the TiO₂/RGO heterostructure

The suspensions of the PDDA-modified TiO₂ nanosheets and GO nanosheets (4:1, weight ratio) were completely blended under stirring. The mixture was centrifuged and freeze-dried. The TiO₂/rGO heterostructure was prepared by annealing the PDDA-TiO₂/GO in N₂ at 500 °C for 2 h.

2.6. Materials characterization

The morphologies and structures of the prepared heterostructures were examined using field emission scanning electron microscopy (FE-

SEM, JEOL, JSM 7610F), transmission electron microscopy (TEM, TECNAI G220 U-Twin instrument), and X-ray crystallography (XRD) using an X-ray diffractometer (Bruker D2 Advance, Cu Kα radiation, λ = 1.5418 Å). The surface area and porosity features of the samples were determined via N₂ adsorption-desorption isotherms at 77 K (Autosorb 6B). The surface compositions of the samples were examined via X-ray photoelectron spectroscopy (XPS) (Thermo ESCALAB 250Xi, Al Kα, hν = 1486.6 eV). The thickness of the nanosheets was measured by atomic force microscopy (AFM) (Asylum MFP-3D). Raman spectra were recorded on a Raman spectrometer (Horiba LabRAM HR Evolution).

2.7. Electrochemical measurements

All electrochemical measurements were conducted on coin cells (size 2032). Home-made sodium foils were used as both the counter and reference electrodes; the working electrode was composed of 70 wt.% of active material, 20 wt.% of acetylene black, and 10 wt.% of carboxymethylcellulose (CMC). The copper disk (diameter = 12 mm) was loaded with active materials (~1.5 mg cm⁻²). NaClO₄ (1 M) in an ethylene carbonate (EC)/diethylene carbonate (DEC) mixture with 5 vol% of fluoroethylene carbonate served as the electrolyte. All coin cells were prepared in an argon-filled glovebox with the moisture and oxygen levels being less than 1 × 10⁻⁶. The CV curves were tested on an electrochemical workstation (CHI760D), while the discharging/charging measurements were conducted on battery analyzers (LAND-CT2001A).

3. Results and discussion

The Ti₃C₂T_x MXene ultrathin nanosheets were finely exfoliated from the bulk Ti₃AlC₂ precursor (Fig. S1) through selectively etching of the Al layers. As shown in Fig. 1(a), the Ti₃C₂T_x MXene supported on lacey carbon exhibits very thin nanosheet structures with sizes of several micrometers. The low-magnification TEM image (Fig. 1(b)) shows that the Ti₃C₂T_x MXene nanosheets become almost transparent to the electron beam. Fig. 1(c) shows the high-resolution TEM (HRTEM) image of the Ti₃C₂T_x MXene nanosheets. After the etching of the Al layers, the Ti₃C₂T_x MXene is exfoliated into single- and few-layered nanoflakes. AFM was performed to explicitly explore the thickness of the Ti₃C₂T_x MXene nanosheet (Figs. 1(d)(e)), revealing a measured height of ~2.0 nm, further verifying its monolayer characteristics [37]. The fluffy Ti₃C₂T_x MXene aerogel (Fig. S2(a)) can be prepared by freeze-drying low-concentration Ti₃C₂T_x MXene dispersions. After annealing the Ti₃C₂T_x MXene aerogel in air conditions, white TiO₂ nanosheets were obtained (Fig. S2(b)). Fig. 1(f) shows the SEM image of Ti₃C₂T_x-derived TiO₂ nanosheets, demonstrating a typical nanosheet morphology and a unique porous structure. Notably, the derived TiO₂ retains its 2D nanosheet structure from the Ti₃C₂T_x precursor (further details are provided in the magnified SEM image in Fig. 1(g)). TiO₂ nanosheets are composed of interconnected TiO₂ nanocrystals, suggesting a confined conversion from Ti₃C₂T_x to TiO₂ nanosheets [33]. The porous characteristics of the TiO₂ nanosheet were further verified by the TEM images (Figs. 1(h)(i)), revealing interconnected nanocrystals with diameters of ~20 nm. The HRTEM image (Fig. 1(i), inset) reveals that TiO₂ exhibits high crystallinity, with the lattice fringe referring to the (101) plane of the anatase TiO₂.

To further explore the structural and compositional changes of the samples, XRD and Raman spectroscopic analyses were conducted before and after the annealing process. As shown in Fig. 1(j), the XRD peaks of the Ti₃C₂T_x MXene disappeared after the annealing treatment and new peaks appeared, attributed to the anatase phase of TiO₂ [27]. This suggests a successful phase conversion from Ti₃C₂T_x to TiO₂ after annealing, which can be further verified by the Raman spectra (Fig. 1(k)). Ti₃C₂T_x MXene exhibits typical Raman shifts located at 201 (A_{1g}), 275 (E_g), 387 (E_g), 595 (E_g), and 715 cm⁻¹ (A_{1g}). After the annealing treatment, new shifts appear at 149 (E_g), 398 (B_{1g}), 526 (A_{1g}), and 642 cm⁻¹ (E_g) in the Raman spectrum, attributed to the characteristic features of

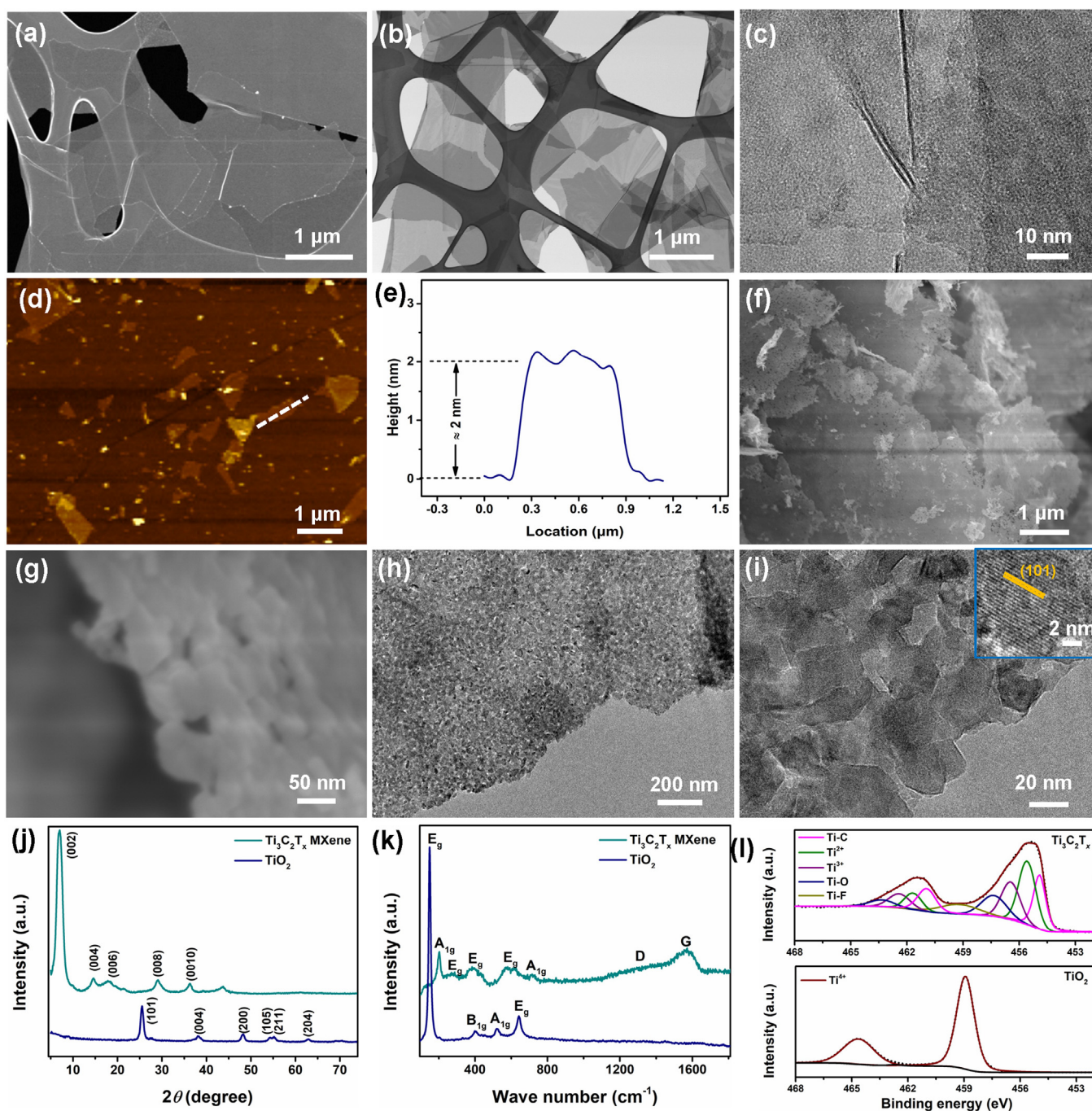


Fig. 1. (a) Scanning electron microscopy (SEM) and (b) Transmission electron microscopy (TEM) images of the $\text{Ti}_3\text{C}_2\text{T}_x$ MXene nanosheets loaded on the lacey carbon. (c) High resolution TEM (HRTEM) image, (d) Atomic force microscopy (AFM) image, and (e) corresponding height profile of the $\text{Ti}_3\text{C}_2\text{T}_x$ MXene nanosheets. (f)(g) SEM images at different magnifications, (h)(i) TEM images, with the inset in (i) HRTEM image of the $\text{Ti}_3\text{C}_2\text{T}_x$ MXene derived TiO_2 nanosheets. Comparisons of (j) XRD patterns, (k) Raman spectra, and (l) XPS spectra of Ti in the $\text{Ti}_3\text{C}_2\text{T}_x$ MXene nanosheets and $\text{Ti}_3\text{C}_2\text{T}_x$ MXene derived TiO_2 nanosheets.

anatase TiO_2 [25]. XPS analysis provided additional evidence supporting this phase transformation. Specifically, the disappearance of peaks associated with the Ti–C, Ti^{2+} , Ti^{3+} , and Ti–F species in $\text{Ti}_3\text{C}_2\text{T}_x$ after annealing (Fig. 1(l)) indicates the removal of carbon and fluorine atoms from the $\text{Ti}_3\text{C}_2\text{T}_x$ structure. This transformation aligns with the conversion of the $\text{Ti}_3\text{C}_2\text{T}_x$ MXene to TiO_2 during annealing. In contrast, the emergence of dominant peaks (Fig. 1(l)) ascribed to Ti^{4+} 2p_{3/2} and Ti^{4+} 2p_{1/2} in TiO_2 further confirms the presence of Ti in its tetravalent oxidation state [27], implying the formation of TiO_2 nanocrystals from the $\text{Ti}_3\text{C}_2\text{T}_x$ precursor.

The intrinsic low electrical conductivity of porous TiO_2 -NSs limits their fast charging/discharging capabilities for Na ions storage, despite presenting a reduced ion diffusion path. Therefore, a TiO_2 /rGO heterostructure assembled by TiO_2 nanosheets and conductive rGO nanosheets was well designed. The entire preparation process of the TiO_2 /rGO heterostructure is presented in Fig. 2(a), where the TiO_2 /rGO heterostructure is prepared through a self-assembly method followed by a post-calcination treatment. Typically, the $\text{Ti}_3\text{C}_2\text{T}_x$ -derived TiO_2 nanosheets are first modified by positively-charged PDDA to afford the TiO_2 /PDDA nanosheet with a positively charged surface. Commer-

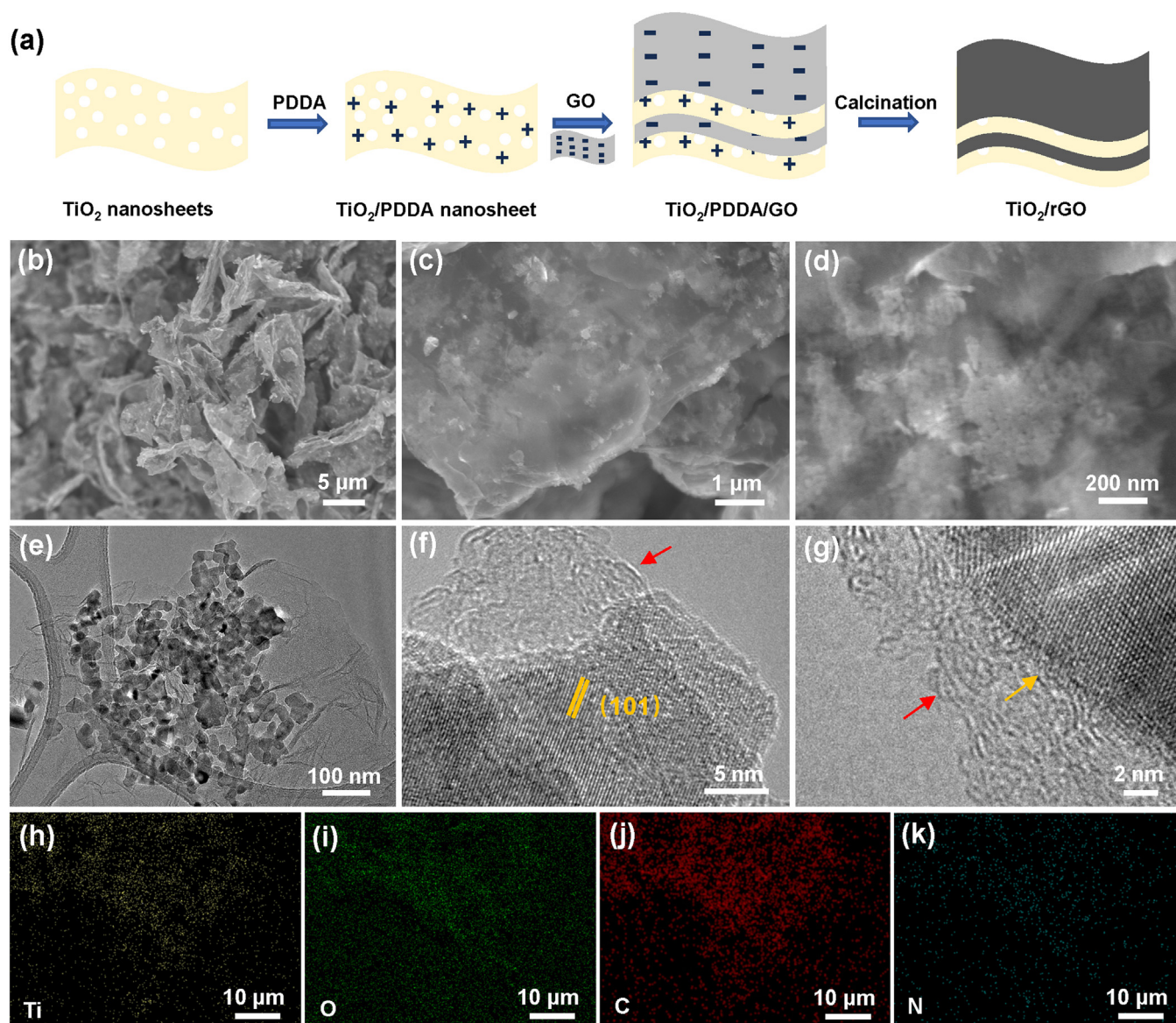


Fig. 2. (a) Schematic synthesis of the TiO_2/rGO heterostructure. (b)–(d) SEM images at different magnifications, (e) TEM image, (f)(g) HRTEM images, and (h)–(k) elemental mapping of the TiO_2/rGO heterostructure.

cial GO is utilized to cooperate with the TiO_2/PDDA nanosheet. Notably, commercial GO nanosheets exhibit a thickness of 1–1.5 nm and a wide range of sizes, spanning from hundreds of nanometers to several micrometers (Fig. S3). When mixed with GO, the positively-charged TiO_2 nanosheets are easily self-assembled with negatively-charged GO to form $\text{TiO}_2/\text{PDDA}/\text{GO}$ due to electrostatic attraction. After the calcination process, the TiO_2/rGO heterostructure is obtained. The detailed microstructure of the self-assembled TiO_2/rGO heterostructure was investigated using FESEM and TEM. The panoramic view of the TiO_2/rGO (Fig. 2(b)) reveals a crumpled 3D structure composed of thin nanosheets. The restacking structure can be observed in Fig. 2(c), in which TiO_2 nanosheets and adjacent rGO form a heterogeneous structure. Fig. 2(d) presents the magnified FESEM image of the self-assembled TiO_2/rGO , where more structural details can be observed. Notably, the porous nanosheet structure of TiO_2 is largely preserved after the annealing treatment, while rGO becomes almost transparent owing to its atomic thickness. The TEM image (Fig. 2(e)) reveals a typical TiO_2/rGO heterostructure in which the mesoporous TiO_2 nanosheet is loaded on an ultrathin rGO nanosheet. The HRTEM image (Fig. 2(f)) shows that

the TiO_2 nanocrystals identified by their typical (101) plane are loaded on an rGO layer (indicated by the red arrow) to form a heterogeneous structure. The interface between the TiO_2 nanocrystals and rGO layers (Fig. 2(g), indicated by the orange arrow) favors the electron and ion transfer. Due to the substantial presence of N species in PDDA, the coupling of GO with PDDA facilitates the carbonization process, resulting in N-doped graphene. In Figs. 2(h)–(k), the good elemental distribution of Ti (yellow), O (green), C (red), and N (cyan) reveals a uniform distribution of TiO_2 and rGO over the entire heterostructure. The interaction between the rGO and TiO_2 nanosheets in the heterostructure plays an essential role in enabling fast charge transport, ultimately attributing superior Na^+ storage properties to SIBs.

After the annealing process, the TiO_2/rGO heterostructure can still maintain the original anatase TiO_2 phase without impurities (Fig. 3(a)), indicating the robustness of the synthetic method and the stability of the heterostructure under thermal treatment. Additionally, the Raman spectrum of the TiO_2/rGO heterostructure shown in Fig. 3(b), confirms the presence of characteristic Raman shifts corresponding to anatase TiO_2 , further supporting the retention of the TiO_2 phase. The appearance of

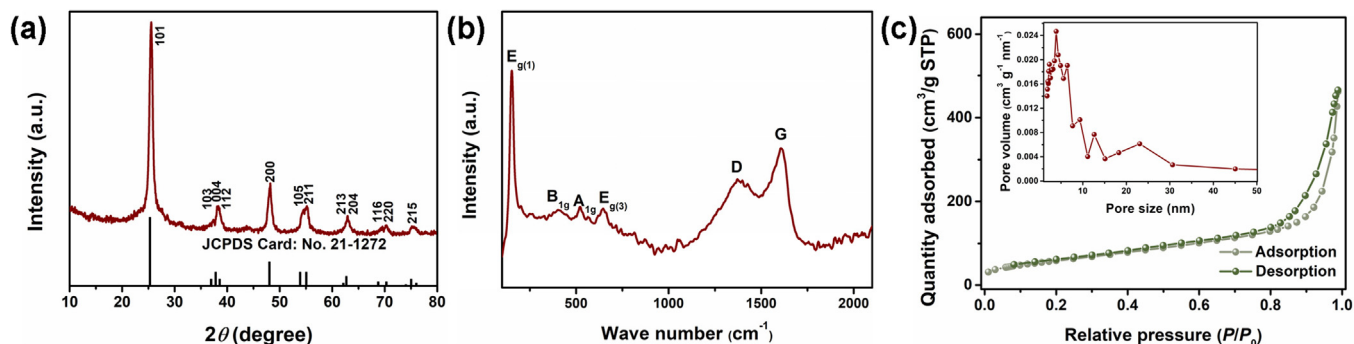


Fig. 3. (a) XRD analysis, (b) Raman spectrum, (c) N_2 adsorption-desorption isotherms, and (c) inset pore size distribution profile of the TiO_2/rGO heterostructure.

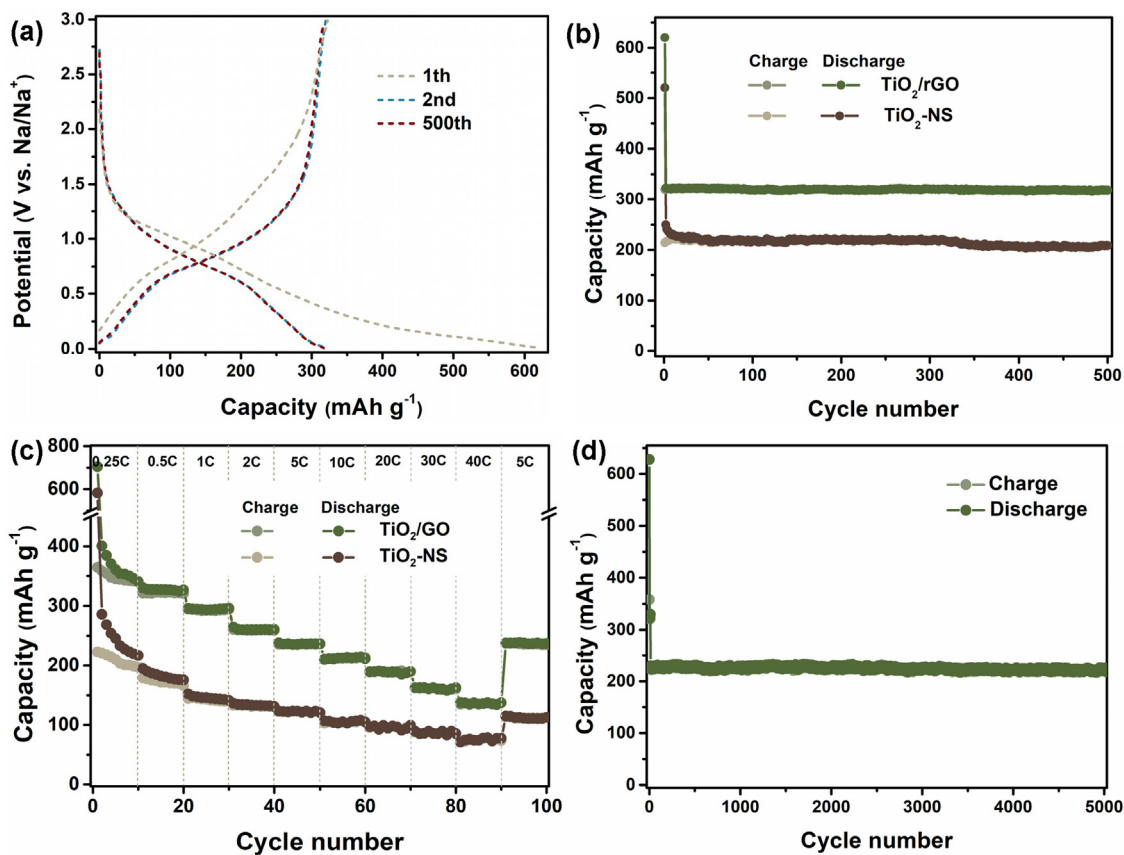


Fig. 4. (a) Charge and discharge voltage profiles of the TiO_2/rGO electrode for selected cycles at 0.5 C. (b) Cycling performance of the TiO_2/rGO and TiO_2-NS electrodes at 0.5 C. (c) Rate behavior of the TiO_2/rGO and TiO_2-NS electrodes. (d) Cycling stability of the TiO_2/rGO electrode at rates of 10 C.

new Raman shifts corresponding to the D and G bands of carbon materials confirms the successful introduction of rGO into the heterostructure. In addition, the TiO_2/rGO heterostructure exhibits a high surface area of $\sim 262 \text{ m}^2 \text{ g}^{-1}$ (Fig. 3(c)) and abundant pores with diverse sizes (Fig. 3(c), inset), implying substantial active sites for Na^+ storage. Overall, the characterization results underscore the structural integrity and compositional purity of the TiO_2/rGO heterostructure, highlighting its enormous potential for SIBs.

The electrochemical behaviors of the TiO_2/rGO as electrode materials for SIBs were further investigated. Fig. S4 presents the cyclic voltammetry (CV) curves (0.01–3.0 V vs. Na^+/Na) of the TiO_2/rGO electrode, revealing irreversible reactions during the initial CV cycle. In the initial cathodic process, a broad reduction peak appeared at 1.05 V, attributed to Ti^{4+} reducing to Ti^{3+} , as well as the formation of a solid-electrolyte interphase (SEI) layer due to electrolyte decomposition [38–40]. Sub-

sequent cycles shifted the reduction peaks to 0.62 V. Oxidation peaks at ~ 0.79 V in both initial and subsequent scans are ascribed to the oxidation of Ti^{3+} to Ti^{4+} . Furthermore, the CV curves of the subsequent cycles exhibit good overlapping, suggesting excellent stability and reversibility of the TiO_2/rGO electrode. In contrast, the CV curves of the TiO_2-NS electrode (Fig. S5) do not overlap, suggesting poor stability and reversibility. Fig. 4(a) presents the voltage profiles (0–3.0 V vs. Na^+/Na) of the TiO_2/rGO electrode during charging/discharging at the 1st, 2nd, and 500th cycles at 0.5 C (1 C = 335 mA g^{-1}). The voltage profiles exhibit reversible sodium ion insertion/extraction at approximately 0.6–0.9 V. However, a higher plateau appears at the initial discharge curve owing to the irreversible reactions. The TiO_2/rGO electrode delivers an initial discharge capacity of 620 mAh g^{-1} and an initial charge capacity of 323 mAh g^{-1} , indicating an initial Coulombic efficiency of 52%. In the subsequent discharge/charge cycles, no significant changes

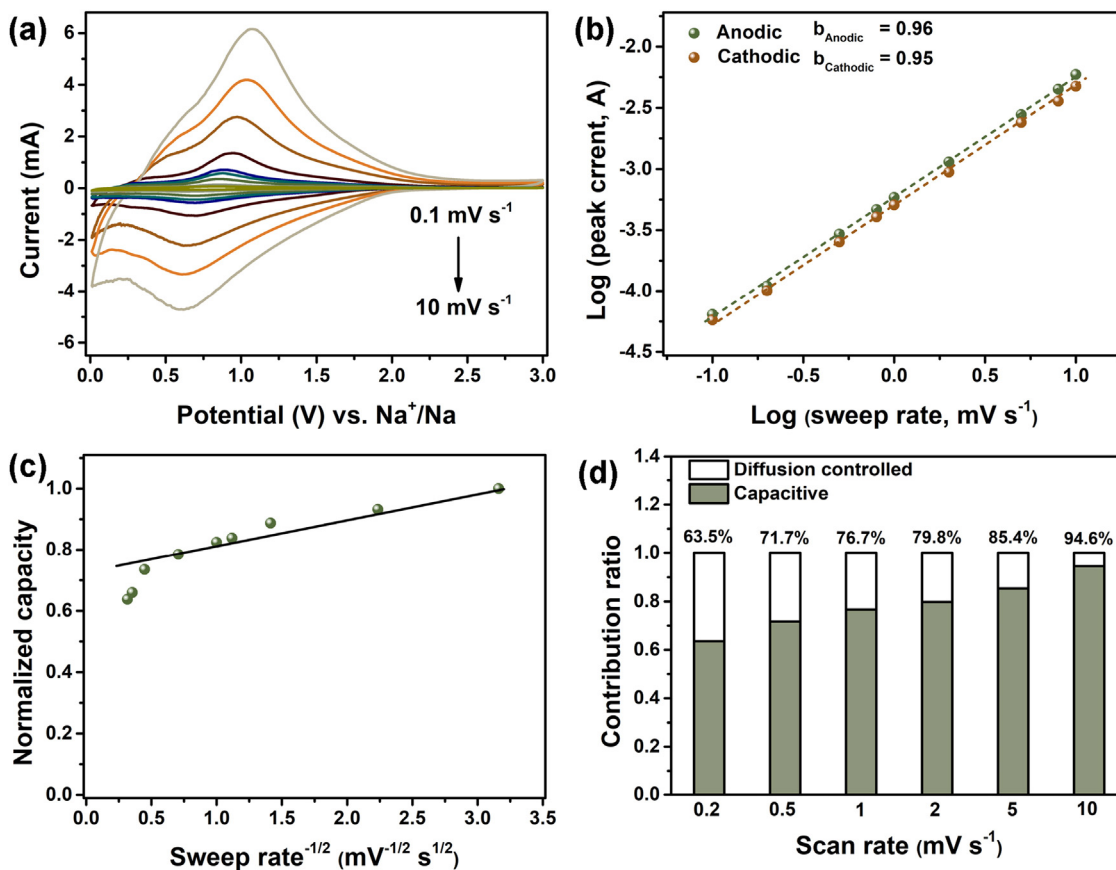


Fig. 5. Reaction kinetics analysis for the TiO₂/rGO electrode: (a) CV curves at various scan rates ranging from 0.1 to 10 mV s⁻¹, (b) Determination of the *b*-value by plotting log(*i*) against log(*v*), (c) Normalized capacity versus sweep rate^{-1/2}, and (d) Calculated charge storage contribution ratio of the capacitive and diffusion-controlled processes at different scan rates.

were observed, demonstrating the high cycling stability of the TiO₂/rGO electrode.

The cycling performance of the TiO₂/rGO electrodes for SIBs was measured at 0.5 C (Fig. 4(b)). The TiO₂/rGO electrode sustained a reversible capacity of 318 mAh g⁻¹ at 0.5 C after 500 cycles, significantly surpassing that of the TiO₂-NS electrode (208 mAh g⁻¹). Fig. 4(c) presents the rate capabilities of the TiO₂/rGO and TiO₂-NS anodes at different current densities (0.25–40 C). At current rates between 0.25–30 C, the TiO₂/rGO electrodes demonstrated superior performance, with capacities of 358, 327, 293, 259, 236, 213, 187, and 160 mAh g⁻¹. Notably, a high capacity of 135 mAh g⁻¹ was achieved even at an ultrahigh rate of 40 C. Upon returning to 5 C, a surprising capacity of 237 mAh g⁻¹ was regained, indicating excellent rate capability. In contrast, the rate capability of the TiO₂-NS electrode was much inferior compared to that of the TiO₂/rGO electrode. The TiO₂-NS electrode experienced rapid capacity fading during high-rate measurements, probably attributed to its sluggish kinetics. Electrochemical impedance spectroscopy (EIS) revealed that the TiO₂/rGO electrode exhibits a smaller charge transfer resistance compared to the TiO₂-NS electrode (Fig. S6), suggesting improved reaction kinetics. Meanwhile, the large phase angle of the inclined line for the TiO₂/rGO electrode implies a significant capacitive behavior during the Na⁺ insertion/extraction process [25,41]. rGO, serving as a continuous-conducting framework, provides fast transport channels for electrons and charges during the Na⁺ insertion/extraction process, and affords more heterogeneous interfaces for extra sodium storage, thereby enabling higher capability. Impressively, at a high current density of 10 C, the TiO₂/rGO electrode presented superior cycling stability (Fig. 4(d)), achieving a reversible capacity of 217 mA h g⁻¹ after 5000 cycles with minimal capacity decay. Table S1

presents a comparison of the TiO₂/rGO electrodes with other similar electrodes reported for SIBs. Notably, the TiO₂/rGO electrode exhibits superior Na⁺ storage properties compared to other electrodes of a similar type.

To further examine the Na⁺ intercalation behavior of the TiO₂/rGO electrode, the reaction kinetics were analyzed through CV measurements (0.1–10 mV s⁻¹) as shown in Fig. 5(a). In the CV curves, the peak current (*i*) and sweep rate (*v*) interact following a power law expression: $i = av^b$ [42], where “*a*” is a proportionality constant and “*b*” is the power-law exponent. A *b*-value of 0.5 indicates a diffusion-controlled process, where the charge transfer is limited by the diffusion of ions within the electrode material. A *b*-value of 1 refers to a surface-controlled (capacitive-like) process, where the charge transfer is limited by the surface reactions. As shown in Fig. 5(b), the *b*-value can be obtained by plotting log(*i*) against log(*v*) for both cathodic and anodic peaks. The obtained *b*-values of 0.96 for the anodic peaks and 0.95 for the cathodic peaks suggest a fast surface-controlled Na⁺ storage process for the TiO₂/rGO electrodes. This indicates that the charge transfer is primarily governed by surface reactions rather than the diffusion of ions within the electrode material. Fig. 5(c) presents the relationship between the normalized capacity and *v*^{-1/2} for the TiO₂/rGO electrodes across a range of sweeps (1–10 mV s⁻¹); the capacity remains nearly unchanged as the scan rates increase at the low-rate range, indicating a surface-controlled capacitive behavior for the charge storage, which is independent of the solid-state sodium-ion diffusion. The electrode’s capacitive behavior dominates the charge storage process, enabling rapid charge/discharge kinetics. Notably, when the sweep rates increase to a high level (above 5 mV s⁻¹), a rapid decrease in the capacity is observed, indicating a diffusion-controlled process where the sodium-

ion diffusion within the electrode material becomes the limiting factor for charge storage [43]. Such findings suggest the interplay between surface-controlled and diffusion-limited processes, which are important factors taken into consideration for optimizing the performance of SIB electrodes.

The quantification of the capacitive and diffusion-controlled charges constituting the entire charge storage at fixed potential and scan rates can be achieved using the equation: $i(V) = k_1v + k_2v^{1/2}$ [25,43]. For instance, at 5 mV s^{-1} , 85.4% of the total charge is calculated to be attributed to the capacitive contribution (Fig. S7), while the remaining portion can be ascribed to diffusion-controlled charges. Similar quantification can be performed at other scan rates, as demonstrated in Fig. 5(d). At 0.2 mV s^{-1} , the capacitive and diffusion contributions are calculated to be 63.5% and 36.5%, respectively. The contribution from the capacitive behavior gradually increases following the increase of the sweep rate, reaching a maximum value of 94.6% at 10 mV s^{-1} and further enhancing the rate capability of the TiO_2/rGO electrode. Compared to diffusion-controlled processes, capacitive storage mechanisms offer faster charge/discharge rates, rendering them particularly advantageous for high-rate applications such as fast charging/discharging in energy storage devices. Therefore, the observed high capacitive contribution is promising for assigning the TiO_2/rGO electrode with excellent rate performance.

The unique heterogeneous structure of TiO_2/rGO significantly contributes to its excellent electrochemical performance. Its mesoporous structure provides a large number of additional Na^+ -storage sites and shortens the pathway of Na^+ diffusion within the electrode material, leading to a higher specific capacity and excellent rate capability. In addition, the conductive rGO network in the TiO_2/rGO heterostructure enhances both electron and Na^+ conductivity, while also mitigating volume expansion during Na^+ insertion/extraction processes. This improves the overall electrochemical reactivity of the electrode.

4. Conclusions

In this study, we present a TiO_2/rGO heterostructure prepared through a self-assembling and post-calcination methods. This heterostructure, composed of restacked mesoporous TiO_2 nanosheets and N-doped rGO nanosheets, was examined as an electrode material for SIBs. Impressively, the TiO_2/rGO electrode delivered a reversible capacity of 318 mAh g^{-1} at 0.5 C for 500 cycles and 215 mAh g^{-1} at 10 C for 5000 cycles. Additionally, the heterostructure rendered the TiO_2/rGO electrodes with a superb rate capability of 135 mAh g^{-1} at 40 C , demonstrating excellent sodium storage properties. The TiO_2/rGO heterostructure combines the advantages of increased active sites, short diffusion pathways, enhanced conductivity, and improved structural stability, resulting in superior electrochemical performance for sodium-ion battery applications. Overall, this study highlights the potential of utilizing engineered structures of 2D materials for advanced energy storage applications.

Declaration of Competing Interests

The authors declare that they have no known competing financial interests or personal relationships that could have appeared to influence the work reported in this paper.

CRedit authorship contribution statement

Baosong Li: Writing – review & editing, Writing – original draft, Visualization, Supervision, Software, Resources, Methodology, Investigation, Conceptualization. **Dezhuang Ji:** Validation, Resources, Investigation. **Abdallah Kamal Hamouda:** Validation, Resources. **Shaohong Luo:** Visualization, Investigation.

Acknowledgements

The authors gratefully acknowledge the financial support provided by the Research & Innovation Center for Graphene and 2D Materials (RIC-2D) and the use of the Khalifa University Core Nanocharacterization Facilities (CNCF).

Supplementary materials

Supplementary material associated with this article can be found, in the online version, at doi:10.1016/j.chphma.2024.05.001.

References

- [1] L. Chen, M. Fiore, J.E. Wang, R. Ruffo, D.K. Kim, G. Longoni, Readiness level of sodium-ion battery technology: A materials review, *Adv. Sustainable Syst.* 2 (2018) 1700153, doi:10.1002/advs.201700153.
- [2] J.Y. Hwang, S.T. Myung, Y.K. Sun, Sodium-ion batteries: Present and future, *Chem. Soc. Rev.* 46 (2017) 3529–3614, doi:10.1039/c6cs00776g.
- [3] F. Liu, X. Cheng, R. Xu, Y. Wu, Y. Jiang, Y. Yu, Binding sulfur-doped Nb_2O_5 hollow nanospheres on sulfur-doped graphene networks for highly reversible sodium storage, *Adv. Funct. Mater.* 28 (2018) 1800394, doi:10.1002/adfm.201800394.
- [4] B. Wang, F. Zhao, G. Du, S. Porter, Y. Liu, P. Zhang, Z. Cheng, H.K. Liu, Z. Huang, Boron-doped anatase TiO_2 as a high-performance anode material for sodium-ion batteries, *ACS Appl. Mater. Inter.* 8 (2016) 16009–16015, doi:10.1021/ac-sami.6b03270.
- [5] G. Fang, Z. Wu, J. Zhou, C. Zhu, X. Cao, T. Lin, Y. Chen, C. Wang, A. Pan, S. Liang, Observation of pseudocapacitive effect and fast ion diffusion in bimetallic sulfides as an advanced sodium-ion battery anode, *Adv. Energy Mater.* 8 (2018) 1703155, doi:10.1002/aenm.201703155.
- [6] Y. Zhou, Y. Liu, M. Zhang, Q. Han, Y. Wang, X. Sun, X. Zhang, C. Dong, J. Sun, Z. Tang, F. Jiang, Rationally designed hierarchical N, P co-doped carbon connected 1T/2H- MoS_2 heterostructures with cooperative effect as ultrafast and durable anode materials for efficient sodium storage, *Chem. Eng. J.* 433 (2022) 133778, doi:10.1016/j.cej.2021.133778.
- [7] F. Niu, J. Yang, N. Wang, D. Zhang, W. Fan, J. Yang, Y. Qian, MoSe_2 -covered N,P-doped carbon nanosheets as a long-life and high-rate anode material for sodium-ion batteries, *Adv. Funct. Mater.* 27 (2017) 1700522, doi:10.1002/adfm.201700522.
- [8] P. Ge, S. Li, L. Xu, K. Zou, X. Gao, X. Cao, G. Zou, H. Hou, X. Ji, Hierarchical hollow-microsphere metal-selenide@carbon composites with rational surface engineering for advanced sodium storage, *Adv. Energy Mater.* 9 (2019) 1803035, doi:10.1002/aenm.201803035.
- [9] F. Song, J. Hu, G. Li, J. Wang, S. Chen, X. Xie, Z. Wu, N. Zhang, Room-temperature assembled MXene-based aerogels for high mass-loading sodium-ion storage, *Nano-Micro Lett* 14 (2021) 37, doi:10.1007/s40820-021-00781-6.
- [10] X. Wang, K. Chen, G. Wang, X. Liu, H. Wang, Rational design of three-dimensional graphene encapsulated with hollow FeP @carbon nanocomposite as outstanding anode material for lithium ion and sodium ion batteries, *ACS Nano* 11 (2017) 11602–11616, doi:10.1021/acsnano.7b06625.
- [11] Y. Jiang, R. Han, J. Dong, R. Yu, S. Tan, F. Xiong, Q. Wei, J. Wang, L. Cui, H. Tian, Y. Yang, Q. An, Uncovering the origin of surface-redox pseudocapacitance of molybdenum phosphides enables high-performance flexible sodium-ion capacitors, *Chem. Eng. J.* 475 (2023) 145962, doi:10.1016/j.cej.2023.145962.
- [12] Z. Huang, H. Hou, Y. Zhang, C. Wang, X. Qiu, X. Ji, Layer-tunable phosphorene modulated by the cation insertion rate as a sodium-storage anode, *Adv. Mater.* 29 (2017) 1702372, doi:10.1002/adma.201702372.
- [13] H. Gao, T. Zhou, Y. Zheng, Y. Liu, J. Chen, H. Liu, Z. Guo, Integrated carbon/red phosphorus/graphene aerogel 3D architecture via advanced vapor-redistribution for high-energy sodium-ion batteries, *Adv. Energy Mater.* 6 (2016) 1601037, doi:10.1002/aenm.201601037.
- [14] D. Luo, J. Xu, Q. Guo, L. Fang, X. Zhu, Q. Xia, H. Xia, Surface-dominated sodium storage towards high capacity and ultrastable anode material for sodium-ion batteries, *Adv. Funct. Mater.* 28 (2018) 1805371, doi:10.1002/adfm.201805371.
- [15] Z. Hong, Y. Zhen, Y. Ruan, M. Kang, K. Zhou, J.M. Zhang, Z. Huang, M. Wei, Rational design and general synthesis of S-doped hard carbon with tunable doping sites toward excellent Na-ion storage performance, *Adv. Mater.* 30 (2018) e1802035, doi:10.1002/adma.201802035.
- [16] S. Feng, K. Li, P. Hu, C. Cai, J. Liu, X. Li, L. Zhou, L. Mai, B.L. Su, Y. Liu, Solvent-free synthesis of hollow carbon nanostructures for efficient sodium storage, *ACS Nano* 17 (2023) 23152–23159, doi:10.1021/acsnano.3c09328.
- [17] C. Yang, S. Xin, L. Mai, Y. You, Materials design for high-safety sodium-ion battery, *Adv. Energy Mater.* 11 (2020) 2000974, doi:10.1002/aenm.202000974.
- [18] H. Kim, H. Kim, Z. Ding, M.H. Lee, K. Lim, G. Yoon, K. Kang, Recent progress in electrode materials for sodium-ion batteries, *Adv. Energy Mater.* 6 (2016) 1600943, doi:10.1002/aenm.201600943.
- [19] S. Lou, Y. Zhao, J. Wang, G. Yin, C. Du, X. Sun, Ti-based oxide anode materials for advanced electrochemical energy storage: Lithium/sodium ion batteries and hybrid pseudocapacitors, *Small* 15 (2019) e1904740, doi:10.1002/sml.201904740.
- [20] L. Chen, K. Guo, S.L. Zeng, L. Xu, C.Y. Xing, S. Zhang, B.J. Li, Cross-stacking aligned non-woven fabrics with automatic self-healing properties for electromagnetic interference shielding, *Carbon* 162 (2020) 445–454, doi:10.1016/j.carbon.2020.02.034.
- [21] Y. Mei, Y. Huang, X. Hu, Nanostructured Ti-based anode materials for Na-ion batteries, *J. Mater. Chem. A* 4 (2016) 12001–12013, doi:10.1039/C6TA04611H.

- [22] H. Xu, Q. Chen, M. Ren, W. Liu, M. Li, G. Li, Titanium glycolate@polythiophene derivative: waxberry-like TiO_2 @carbon composites with high-pseudo-capacitive performance for sodium storage, *J. Electrochem. Soc.* 166 (2019) A1096–A1102, doi:10.1149/2.0651906jes.
- [23] H. Xiong, M.D. Slater, M. Balasubramanian, C.S. Johnson, T. Rajh, Amorphous TiO_2 nanotube anode for rechargeable sodium ion batteries, *J. Phys. Chem. Lett.* 2 (2011) 2560–2565, doi:10.1021/jz2012066.
- [24] K. Lan, Y. Liu, W. Zhang, Y. Liu, A. Elzatahry, R. Wang, Y. Xia, D. Al-Dhayan, N. Zheng, D. Zhao, Uniform ordered two-dimensional mesoporous TiO_2 nanosheets from hydrothermal-induced solvent-confined monomicelle assembly, *J. Am. Chem. Soc.* 140 (2018) 4135–4143, doi:10.1021/jacs.8b00909.
- [25] B. Li, B. Xi, Z. Feng, Y. Lin, J. Liu, J. Feng, Y. Qian, S. Xiong, Hierarchical porous nanosheets constructed by graphene-coated, interconnected TiO_2 nanoparticles for ultrafast sodium storage, *Adv. Mater.* 30 (2018) 1705788, doi:10.1002/adma.201705788.
- [26] Z. Le, F. Liu, P. Nie, X. Li, X. Liu, Z. Bian, G. Chen, H.B. Wu, Y. Lu, Pseudocapacitive sodium storage in mesoporous single-crystal-like TiO_2 -graphene nanocomposite enables high-performance sodium-ion capacitors, *ACS Nano* 11 (2017) 2952–2960, doi:10.1021/acsnano.6b08332.
- [27] B. Li, S. Anwer, X. Huang, S. Luo, J. Fu, K. Liao, Nitrogen-doped carbon encapsulated in mesoporous TiO_2 nanotubes for fast capacitive sodium storage, *J. Energy Chem.* 55 (2021) 202–210, doi:10.1016/j.jechem.2020.06.074.
- [28] F. Shahzad, M. Alhabeab, C.B. Hatter, B. Anasori, S.M. Hong, C.M. Koo, Y. Gogotsi, Electromagnetic interference shielding with 2D transition metal carbides (MXenes), *Science* 353 (2016) 1137–1140, doi:10.1126/science.aag2421.
- [29] S. Luo, T. Alkhidir, S. Mohamed, S. Anwer, B. Li, J. Fu, K. Liao, V. Chan, Investigation of interfacial interaction of graphene oxide and $\text{Ti}_3\text{C}_2\text{T}_x$ (MXene) via atomic force microscopy, *Appl. Surf. Sci.* 609 (2023) 155303, doi:10.1016/j.apsusc.2022.155303.
- [30] C. Bao, J. Wang, B. Wang, J. Sun, L. He, Z. Pan, Y. Jiang, D. Wang, X. Liu, S.X. Dou, J. Wang, 3D sodiophilic Ti_3C_2 MXene@g- C_3N_4 hetero-interphase raises the stability of sodium metal anodes, *ACS Nano* 16 (2022) 17197–17209, doi:10.1021/acsnano.2c07771.
- [31] Q. Han, C. Wu, H. Jiao, R. Xu, Y. Wang, J. Xie, Q. Guo, J. Tang, Rational design of high-concentration Ti^{3+} in porous carbon-doped TiO_2 nanosheets for efficient photocatalytic ammonia synthesis, *Adv. Mater.* 33 (2021) 2008180, doi:10.1002/adma.202008180.
- [32] H. Zhang, L. Yang, P. Zhang, C. Lu, D. Sha, B. Yan, W. He, M. Zhou, W. Zhang, L. Pan, Z. Sun, MXene-derived TiO_{2n-1} quantum dots distributed on porous carbon nanosheets for stable and long-life Li-S batteries: Enhanced polysulfide mediation via defect engineering, *Adv. Mater.* 33 (2021) 2008447, doi:10.1002/adma.202008447.
- [33] R. Li, X. Ma, J. Li, J. Cao, H. Gao, T. Li, X. Zhang, L. Wang, Q. Zhang, G. Wang, C. Hou, Y. Li, T. Palacios, Y. Lin, H. Wang, X. Ling, Flexible and high-performance electrochromic devices enabled by self-assembled 2D TiO_2 /MXene heterostructures, *Nat. Commun.* 12 (2021) 1587, doi:10.1038/s41467-021-21852-7.
- [34] T. Wu, P.R.C. Kent, Y. Gogotsi, D.E. Jiang, How water attacks MXene, *Chem. Mater.* 34 (2022) 4975–4982, doi:10.1021/acs.chemmater.2c00224.
- [35] S. Chertopalov, V.N. Mochalin, Environment-sensitive photoresponse of spontaneously partially oxidized Ti_3C_2 MXene thin films, *ACS Nano* 12 (2018) 6109–6116, doi:10.1021/acsnano.8b02379.
- [36] S. Ahmed, B. Li, S. Luo, K. Liao, Heterogeneous $\text{Ti}_3\text{C}_2\text{T}_x$ MXene-MWCNT@ MoS_2 film for enhanced long-term electromagnetic interference shielding in the moisture environment, *ACS Appl. Mater. Inter.* 15 (2023) 49458–49467, doi:10.1021/ac-sami.3c08279.
- [37] B. Li, S. Luo, S. Anwer, V. Chan, K. Liao, Heterogeneous films assembled from $\text{Ti}_3\text{C}_2\text{T}_x$ MXene and porous double-layered carbon nanosheets for high-performance electromagnetic interference shielding, *Appl. Surf. Sci.* 599 (2022) 153944, doi:10.1016/j.apsusc.2022.153944.
- [38] R. Luo, Y. Ma, W. Qu, J. Qian, L. Li, F. Wu, R. Chen, High pseudocapacitance boosts ultrafast, high-capacity sodium storage of 3D graphene foam-encapsulated TiO_2 architecture, *ACS Appl. Mater. Inter.* 12 (2020) 23939–23950, doi:10.1021/ac-sami.0c04481.
- [39] Y. Lu, N. Zhang, S. Jiang, Y. Zhang, M. Zhou, Z. Tao, L.A. Archer, J. Chen, High-capacity and ultrafast Na-ion storage of a self-supported 3D porous antimony persulfide-graphene foam architecture, *Nano Lett.* 17 (2017) 3668–3674, doi:10.1021/acs.nanolett.7b00889.
- [40] Z.L. Xu, K. Lim, K.Y. Park, G. Yoon, W.M. Seong, K. Kang, Engineering solid electrolyte interphase for pseudocapacitive anatase TiO_2 anodes in sodium-ion batteries, *Adv. Funct. Mater.* 28 (2018) 1802099, doi:10.1002/adfm.201802099.
- [41] B. Li, B. Xi, F. Wu, H. Mao, J. Liu, J. Feng, S. Xiong, One-step in situ formation of N-doped carbon nanosheet 3D porous networks/ TiO_2 hybrids with ultrafast sodium storage, *Adv. Energy Mater.* 9 (2019) 1803070, doi:10.1002/aenm.201803070.
- [42] V. Augustyn, J. Come, M.A. Lowe, J.W. Kim, P.L. Taberna, S.H. Tolbert, H.D. Abruña, P. Simon, B. Dunn, High-rate electrochemical energy storage through Li^+ intercalation pseudocapacitance, *Nat. Mater.* 12 (2013) 518–522, doi:10.1038/nmat3601.
- [43] C. Chen, Y. Wen, X. Hu, X. Ji, M. Yan, L. Mai, P. Hu, B. Shan, Y. Huang, Na^+ intercalation pseudocapacitance in graphene-coupled titanium oxide enabling ultra-fast sodium storage and long-term cycling, *Nat. Commun.* 6 (2015) 6929, doi:10.1038/ncomms7929.